Journal of Materials Chemistry A

ROYAL SOCIETY OF CHEMISTRY

PAPER

View Article Online
View Journal



Cite this: DOI: 10.1039/d5ta09301e

# Defect passivation by annealing enables stable transport in Li-doped $Mg_2Sn$ epitaxial films for microfabricated thermoelectric devices

Kenneth Magallon Senados, [abc] Takashi Aizawa,[b] Isao Ohkubo, [ab] Masayuki Murata,[d] Takahiro Baba,[ab] Akihiko Ohi,[e] Akira Uedono,[a] Takeaki Sakurai *[af] and Takao Mori *[ab]

Li-doped $Mg_2Sn$ thin films are promising p-type thermoelectrics, as Li is among the most effective acceptors, yet their impact on defect chemistry, phase stability, and transport remains poorly understood. Here, low-temperature annealing is shown to passivate Li-induced defects and stabilize electrical transport in epitaxial $Mg_{2-x}Li_xSn$ ($0 \leq x \leq 0.10$) thin films grown by molecular beam epitaxy. X-ray diffraction and electron microscopy reveal that Li incorporation produces Sn-rich precipitates from deviation from the 2 : 1 of Mg : Sn stoichiometry, which are partially dissolved after annealing. Depth-resolved positron annihilation spectroscopy indicates a reduction of Mg-vacancy-type defects at moderate Li content, while Hall measurements show decreased hole concentrations and enhanced mobilities, consistent with reduced ionized-impurity scattering. As-grown films exhibit Seebeck coefficients of 40–70 $\mu V\ K^{-1}$ at room temperature, which increase to ~200–250 $\mu V\ K^{-1}$ after annealing, accompanied by suppression of cycle-to-cycle drift. The optimized films achieve an exceptional peak power factor of ~$2.4 \times 10^{-3}$ $W\ m^{-1}\ K^{-2}$ at the relatively low temperature of 350 K. Thermal conductivity, measured at room temperature, confirms that defect-engineered films retain strong phonon scattering after annealing, yielding $zT \approx 0.25$, surpassing prior p-type $Mg_2Sn$ epitaxial thin films. A microfabricated π-type thermoelectric generator using Li-doped $Mg_2Sn$ p-legs delivers higher open-circuit voltage than a $Mg_2Sn$(Ge) benchmark with comparable output power, demonstrating the practical viability of the processed films.

Received 15th November 2025
Accepted 1st February 2026

DOI: 10.1039/d5ta09301e

rsc.li/materials-a



## 1 Introduction

Thin-film thermoelectric generators are emerging as compact, maintenance-free power sources for Internet-of-Things sensors and on-chip cooling applications, where miniaturized device geometries and rapid thermal response are essential.[1–6] By directly converting heat into electricity without chemical reactions or moving components, thermoelectric generators based on films combine durability with long-term operational stability, making them well-suited for harsh or inaccessible environments.[7–9] In these thermoelectric films, electronic and phononic transport occur over length scales comparable to film thickness and feature sizes, so even slight variations in vacancy concentration or the presence of nanometer-scale secondary phases can markedly change electrical conductivity $\sigma$ and Seebeck coefficient $S$.[10,11] Because the power factor $S^2\sigma$ directly determines the thermoelectric figure of merit $zT$, precise control over point and extended defects is essential to optimize thin-film performance for IoT and micro-power architectures.[12]

Among lead-free thermoelectric systems, $Mg_2Sn$ stands out for its earth abundance, non-toxicity, and compatibility with silicon-based technologies. Numerous studies have reported intrinsic defects in $Mg_2Sn$, including Mg vacancies, antisite defects, and vacancy clusters, which strongly influence carrier transport and thermoelectric properties.[13–15] While n-type $Mg_2Sn$ regularly achieves high $zT$ values around ~1.4, the performance of bulk p-type $Mg_2Sn$ remains limited (typically $zT < 0.7$) due to native defects that compensate acceptor dopants and suppress hole conduction.[16,17] Lithium substitution on Mg sites has been shown to effectively mitigate these intrinsic vacancies in bulk samples, enhancing the Seebeck coefficient up to approximately 200 $\mu VK^{-1}$.[18–20] However, excessive Li incorporation can lead to the formation of Sn-rich secondary

[a]Graduate School of Pure and Applied Sciences, University of Tsukuba, 1-1-1 Tennodai, Tsukuba, Ibaraki 305-8573, Japan. E-mail: sakurai.takeaki.ft@u.tsukuba.ac.jp
[b]Research Center for Materials Nanoarchitectonics (MANA), National Institute for Materials Science (NIMS), 1-1 Namiki, Tsukuba, Ibaraki 305-0044, Japan. E-mail: MORI.Takao@nims.go.jp
[c]Department of Physics, University of Science and Technology of Southern Philippines, C.M. Recto Avenue Lapasan, Cagayan de Oro 9000, Philippines
[d]Research Institute for Energy Conservation, National Institute of Advanced Industrial Science and Technology (AIST), 1-1-1 Umezono, Tsukuba, Ibaraki 305-8568, Japan
[e]Nanotechnology Innovation Station, National Institute for Materials Science (NIMS), 1-1 Namiki, Tsukuba, Ibaraki 305-0044, Japan
[f]Tsukuba Institute for Advanced Research (TIAR), University of Tsukuba, 1-1-1 Tennodai, Tsukuba, Ibaraki, 305-8577, Japan

phases, signaling a solubility limit and complicating defect control.[19] Therefore, understanding the behavior and control of Li-induced defects in $Mg_2Sn$ thin films is crucial for their successful integration as stable p-type components in miniature thermoelectric devices.

In epitaxial $Mg_2Sn$ films, growth-related factors such as surface migration kinetics, epitaxial strain, and nonequilibrium incorporation pathways can introduce defect channels and alter dopant solubility relative to bulk, making dopant behavior more complex.[12,21–23] Notably, Li-doped $Mg_2Sn$ epitaxial thin films have not yet been explored and our initial molecular-beam epitaxy (MBE) trials conducted for this work have indicated possible instability, showing noticeable cycle-to-cycle variations in electrical conductivity and Seebeck coefficient in the doped samples. Such preliminary findings point to the likely existence of metastable, film-specific defects, motivating a detailed investigation to understand their origins and dynamics, and ultimately enable stable, high-performance p-type thermoelectric films.

Low-temperature post-growth annealing is a proven method to improve thin film performance. In semiconductors, it can activate dopants, remove metastable defects, and regulate vacancy populations without exceeding temperatures that risk phase changes or loss of film integrity.[24–27] By enabling limited atomic motion, such treatments allow defects to diffuse, recombine, or transform into less harmful states, improving stability without altering the as-grown structure. In thermoelectric thin films, where carrier and phonon transport are highly sensitive to defects, controlled annealing can shift scattering mechanisms, reduce drift in transport properties, and enhance device reliability.[28–32] For epitaxial films, the process preserves crystallographic alignment and interface quality while enabling targeted defect engineering.[33,34] For $Mg_2Sn$-based materials, this approach offers an attractive route to mitigate Li-induced disorder without triggering Mg–Sn interdiffusion or the nucleation of new secondary phases. In this work, we examine the potential of a moderate thermal anneal at 473 K to eliminate Li-induced Sn-rich precipitates, passivate vacancy-type defects, and stabilize carrier transport in Li-doped $Mg_2Sn$ epitaxial films, thereby linking targeted defect control to reproducible and application-ready thermoelectric performance.

In this work, we grow 300 nm $Mg_{2-x}Li_xSn$ ($0 \le x \le 0.10$) films on a mirror-polished sapphire(0001) single crystal wafers by MBE, apply a one-hour annealing at 473 K under high vacuum, and tracked structural, defect, and transport changes using X-ray diffraction, scanning electron microscopy, positron annihilation spectroscopy, Hall, and temperature-cycled Seebeck/conductivity measurements. Finally, we demonstrate device-level viability by microfabrication of a π-type thermoelectric module from our processed films, showing stable performance under practical temperature gradients.

## 2 Experiment and methods

$Mg_{2-x}Li_xSn$ ($0 \le x \le 0.10$) epitaxial thin films of average thickness ~300 nm were grown on sapphire (0001) substrates using a conventional ultrahigh vacuum (UHV) MBE apparatus (Eiko, EV-500) under vacuum conditions of $10^{-6}$–$10^{-7}$ Pa.[35] Substrates were ultrasonically cleaned in acetone and subsequently degassed at 1000 °C for 1 h prior to deposition. Films were deposited at 400 °C for 30 min using elemental Mg (>99.95%), Sn (>99.999%), and Li (>99.9%) sources evaporated from effusion cells. The Mg flux was set to 15.0 atoms $s^{-1}$ $nm^{-2}$ based on optimized growth conditions from our previous study.[12] To achieve $Mg_{2-x}Li_xSn$ ($0 \le x \le 0.10$), the Li flux replaced an equivalent fraction of the Mg flux, while the Sn flux was held constant at 1.60 atoms $s^{-1}$ $nm^{-2}$. The Mg, Sn, and Li compositions used in this work were calculated from the respective beam fluxes and the growth rate obtained from MBE flux calibration, assuming complete incorporation; thus, the reported compositions represent nominal values derived from the deposition conditions rather than absolute atomic fractions. The full list of growth conditions, including sample compositions, flux rates, and effusion cell temperatures, is summarized in SI Table S1. The grown films were divided into two sets, with one set subjected to post-growth annealing in a custom-built horizontal quartz-tube furnace. Samples were placed on a quartz boat inside the evacuated quartz tube and heated at 473 K for 1 h under dynamic vacuum (~$1 \times 10^{-2}$ Pa), maintained by continuous turbomolecular pumping. This relatively low annealing temperature was selected to minimize Mg loss from the $Mg_2Sn$ films. No gases were intentionally introduced during heating or cooling. Structural characterization included X-ray diffraction (Rigaku SmartLab) and transmission electron microscopy (TEM, Talos F200X, 200 kV). Vacancy-type defects were probed using positron annihilation spectroscopy (PAS). Details of the PAS technique are described elsewhere.[36–39] Thermoelectric properties were evaluated by measuring the Seebeck coefficient and electrical conductivity (ZEM-3) and conducting Hall measurements for carrier concentration and mobility. Cross-plane thermal conductivity was measured using a picosecond time-domain thermoreflectance (TDTR) system in a front-heating/front-detection configuration (Netzsch- Geratebau GmbH), following procedures described in previous reports.[40–42] Thermal conductivity ($\kappa$) was calculated as $\kappa = \lambda \cdot d \cdot C_p$, where $\lambda$ is the thermal diffusivity, $d$ is the density, and $C_p$ is the specific heat capacity at constant pressure of $Mg_2Sn$.[43] Thermoelectric π-type devices consisting of Li-doped $Mg_2Sn$ as the p-type legs and Bi as the n-type legs were fabricated following the microfabrication framework established for $Mg_2Sn$-based thin film, with modifications to the etching step.[44,45] Standard photolithography techniques were used to define the device geometry, after which the Li-doped $Mg_2Sn$ films were patterned by reactive ion etching in a $BCl_3$/Ar plasma, replacing the argon-ion milling and reactive ion etching (RIE) sequence reported by the previous study. The n-type Bi legs were deposited at room temperature by electron-beam evaporation to preserve microstructural integrity, with a thickness of approximately 300 nm. For the Bi legs, the thermoelectric parameters established in the previous $Mg_2Sn_{0.80}Ge_{0.20}$/Bi device analysis were a resistivity of ~$1.1 \times 10^{-6}$ Ωm and a Seebeck coefficient ~−40 μV $K^{-1}$.[45] Electrical contacts were formed by electron-beam evaporation of a Cr/Ni/

 

Pt tri-layer and patterned *via* lift-off. Device performance was characterized under controlled temperature gradients in vacuum.

# 3 Results and discussion

## 3.1 Structural and phase evolution

The XRD patterns of all samples exhibit strong $Mg_2Sn$ (*nnn*) peaks ($n = 1-4$), indexable to the cubic antifluorite structure ($Fm\bar{3}m$). XRD patterns of $Mg_{2-x}Li_xSn$ films ($x = 0.05$, 0.08, 0.10) in Fig. 1a show these dominant peaks, while all Li levels also exhibit weak additional reflections at $2\theta \approx 30.6°$ and 31.8°, assignable to the (101) and (110) planes of metallic Sn. The intensity of these Sn-related peaks increases with Li content, indicating progressive Li-induced supersaturation and Sn segregation even at the lowest achievable doping level ($x = 0.05$). The absence of data for $x < 0.05$ reflects an intrinsic MBE limitation: the Li effusion cell cannot reliably deliver fluxes below $x = 0.05$ without falling below its thickness-monitor detection limit. Efforts to offset this by increasing the Mg flux led to degraded crystallinity and poor epitaxy, consistent with prior results.[12]

As shown in Fig. 1b, Li incorporation into the $Mg_2Sn$ lattice shifts the $Mg_2Sn$(111) diffraction peak toward higher $2\theta$ relative to the undoped reference, indicating a reduction in lattice parameter according to Bragg's law. This trend is consistent with predominantly substitutional occupation of Mg sites by Li, whose atomic radius (152 pm) is smaller than that of Mg (160 pm). Although Li is small, interstitial incorporation in $Mg_2Sn$ is not necessarily favored because site occupancy is governed primarily by defect formation energetics and charge compensation. Hybrid-DFT defect calculations by Kamila *et al.* identify substitutional Li on Mg sites, $Li_{Mg}$, as an acceptor-type defect relevant to p-type doping.[46] The same calculations show that interstitial Li, $Li_{int}$, is donor-type and acts as a compensating defect channel. A significant $Li_{int}$ population would counteract acceptor doping, which thermodynamically self-limits the steady-state interstitial fraction under p-type conditions. Therefore, interstitial Li is not expected to be the dominant incorporated configuration in this study. Even if a minor $Li_{int}$ fraction is present, it would not control the average lattice parameter measured by XRD, consistent with the net lattice contraction inferred from the (111) peak shift.

In the as-grown state (Fig. 1b), the $x = 0.10$ $Mg_{2-x}Li_xSn$ film however shows a slight displacement of the (111) peak toward lower $2\theta$ compared with the $x = 0.05$ and $x = 0.08$ films, which may suggest local lattice expansion from defect-induced strain and a higher presence of Sn-rich phases at the highest Li concentration. Post-growth annealing at 473 K for 1 h under vacuum ($\sim 10^{-2}$ Pa) produces a systematic shift of the (111) peak to higher $2\theta$ for all Li-doped films relative to their unannealed positions, consistent with further lattice contraction. At 473 K, the equilibrium vapor pressure of elemental Mg, estimated from standard solid-Mg vapor-pressure data, is on the order of $10^{-8}$ Torr, substantially lower than the background pressure, so substantial Mg loss from the dense $Mg_2Sn$ films during this 1 h anneal is not expected from thermodynamic considerations.[47] Consistent with this expectation, cross-sectional TEM–EDS performed on the nominal 5% Li film shows that the Mg/Sn atomic ratio in the $Mg_2Sn$ matrix region (Area #1; Fig. S2) remains essentially unchanged after annealing (Mg/Sn = 1.88 as-grown *vs.* 1.89 annealed; Table S2). Although EDS cannot quantify Li, these results indicate that, at least for this representative nominal 5% Li film, the annealing-induced changes in

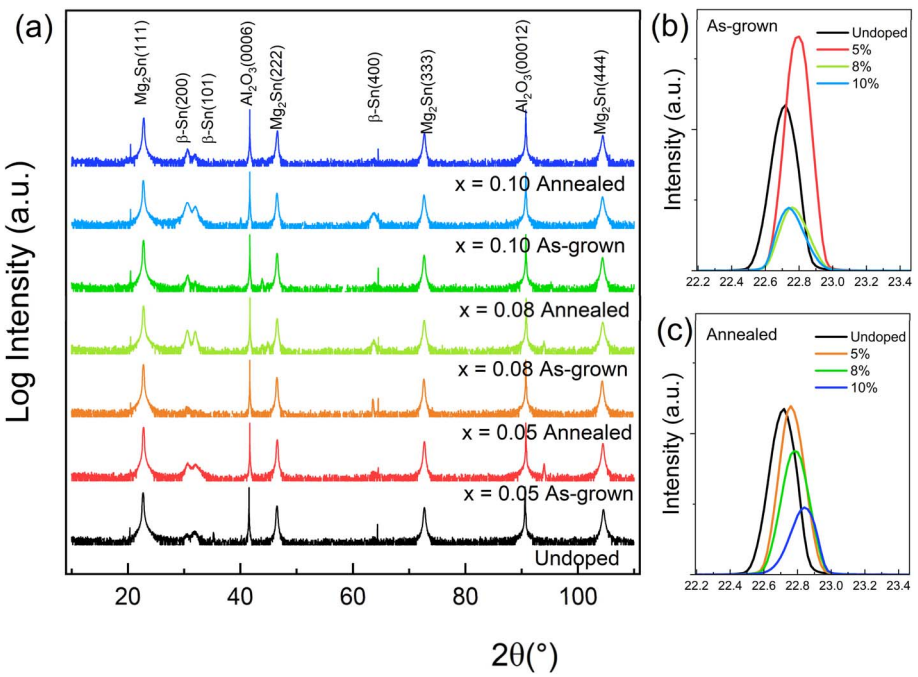


Fig. 1 (a) X-ray diffraction patterns of $Mg_{2-x}Li_xSn$ films before and after annealing at 200 °C, (b) as-grown and (c) annealed $Mg_2Sn$ (111) peak.

transport properties are unlikely to arise from a deviation in Mg/Sn stoichiometry due to Mg loss, and are instead consistent with Li-related defect/phase reorganization. This change is therefore attributed to more complete Li substitution on Mg sites and the reorganization or partial dissolution of lattice-expanding defects and secondary phases, including Sn-rich regions. In the logarithmic XRD patterns in Fig. 1a, the $Mg_2Sn$ fundamental reflections remain the dominant film peaks for all Li contents, their positions are unchanged by annealing within the instrumental resolution, and no additional Mg-deficient secondary phases are detected, indicating that the $Mg_2Sn$ phase fraction is not strongly reduced by annealing and that the overall Mg : Sn ratio is preserved within the sensitivity of XRD.

Secondary Sn phases have also been reported in Ga-doped $Mg_2Sn$, however *via* a different mechanism.[22] Ga's low solubility produces Ga droplets that disrupt adatom migration during growth and indirectly promote Sn precipitation. In Li-doped films, Sn segregation is likely associated with locally Mg-poor (Sn-rich) growth conditions induced by Li incorporation, rather than a reduced Mg supply rate. Although the Mg flux was kept approximately constant, Li can perturb Mg incorporation kinetics at the growth front, for example by modifying surface transport and reducing Mg sticking and/or enhancing Mg re-evaporation due to the high volatility of Mg. This can shift the local composition toward the Mg-deficient, Sn-rich side of the Mg–Sn phase diagram.[48,49] Under Mg-poor conditions, the equilibrium state falls in the $Mg_2Sn$ + β-Sn two-phase region, so surplus Sn can no longer be accommodated in the antifluorite $Mg_2Sn$ lattice and segregates as β-Sn precipitates. Sn-rich precipitates have also been reported in Li-doped $Mg_2Sn$ single crystals (bulk), supporting the plausibility of Sn segregation in Li-containing $Mg_2Sn$ under Sn-rich conditions. Post-growth annealing at 473 K for 1 h under vacuum partially suppressed the Sn-related reflections. This suppression could indicate that annealing at 473 K increases atomic mobility and promotes local redistribution of Mg and Sn in the thin film. Because $Mg_2Sn$ is thermodynamically favored near the intended composition, this redistribution can reduce Sn segregation and consume part of the β-Sn phase through $Mg_2Sn$ formation, effectively incorporating Sn into the $Mg_2Sn$ lattice and lowering the β-Sn contribution to the XRD intensity. Although secondary peak intensities in XRD decreased, residual Sn signals persisted at higher Li levels ($x \geq 0.08$), indicating only partial reabsorption of Sn into the $Mg_2Sn$ matrix and suggesting that a fraction of Sn-rich regions remain stabilized against present annealing conditions. Because the film compositions discussed here are nominal values derived from calibrated MBE fluxes and we did not perform global stoichiometry measurements such as XRF or RBS, our interpretation of Sn segregation and its evolution upon annealing relies on structural signatures from XRD together with local compositional evidence. To directly support this point, we next present SEM and cross-sectional TEM combined with EDX mapping, which reveal Sn-rich, Mg-depleted regions and their redistribution upon annealing.

SEM and TEM of the $x = 0.05$ Li content samples provide complementary insight into these changes. In the as-grown $x = 0.05$ film (Fig. 2a), numerous bright particulates 100–500 nm in diameter appear on the surface, confirmed by cross-sectional TEM and EDX mapping to be Sn-rich, Mg-depleted inclusions near the free surface. No similar clusters are found deeper in the film. Their presence at the growth surface is consistent with limited adatom mobility and the Li-induced shift toward Sn-rich composition identified in XRD analysis. Although the MBE growth temperature (~400 °C) is well below the Mg–Sn eutectic temperature,[49] local composition can still shift enough to favor Sn-rich regions under Li doping and limited Mg flux. Under these conditions, restricted surface diffusion promotes surface-proximal nucleation, allowing excess Sn to accumulate at the growth surface. After annealing (Fig. 2b), these particulates diminish in size and contrast, and TEM reveals a more homogeneous Mg and Sn distribution, although residual Sn-rich regions remain. The changes point to partial redistribution and morphological transformation of Sn phases rather than their complete elimination.

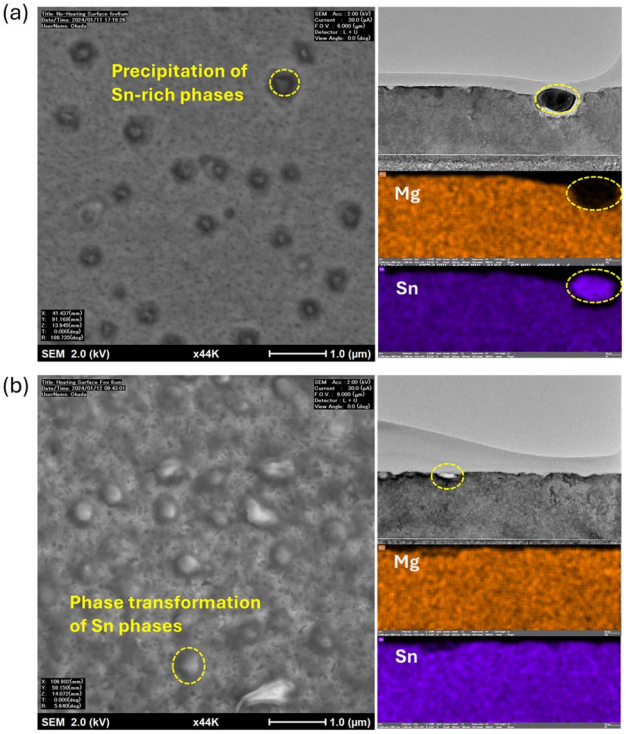


Fig. 2 Surface and cross-sectional microstructures of $Mg_{1.95}Li_{0.05}Sn$ film ($x = 0.05$): (a) as-grown and (b) annealed at 473 K for 1 h obtained by SEM, TEM, and EDX mapping. Sn rich regions are visible near the film surface.

Although the annealing was carried out in a quartz-tube furnace under dynamic vacuum (~$1 \times 10^{-2}$ Pa) with no intentional gas introduction, such conditions inevitably contain trace residual species such as $O_2$, $H_2O$, and $H_2$ released from the chamber walls and pumping line. Even at very low partial pressures these molecules can interact with Li-related defects. A plausible pathway is that Li interstitials or Li-vacancy complexes are converted into more stable configurations, such as substitutional Li on Mg sites or neutral Li–O/Li–H complexes. These localized reactions could suppress lattice-expanding defects

 

without producing detectable oxide phases, consistent with the observed lattice contraction and partial reabsorption of Sn-rich regions. Similar atmosphere-assisted effects have been reported in other semiconductors, where residual gases present during vacuum annealing influenced lattice parameters and defect parameters.[50] By contrast, when the same 473 K anneal was carried out in the MBE chamber under UHV immediately after growth without air exposure, the transport properties remained essentially similar to those of the as-grown films (SI Fig. S3), underscoring that residual gas chemistry under low-vacuum conditions is required to drive the structural and electronic recovery observed in this work.

### 3.2 Vacancy-type defect characterization

Depth-resolved positron annihilation spectroscopy (PAS) was employed to investigate vacancy-type defects in $Mg_{2-x}Li_xSn$ films in their as-grown state and after annealing. PAS measurements were performed for the undoped $Mg_2Sn$ film and for two representative Li-doped compositions ($x = 0.05$ and $x = 0.10$) in both as-grown and annealed states, in order to track defect evolution between the undoped limit and the highest Li content. Fig. 3 presents *S*-parameter profiles across implantation depths covering the full film thickness (~300 nm). The *S*-parameter reflects the momentum distribution of annihilating positron-electron pairs and is highly sensitive to open-volume defects such as vacancies. In Doppler-broadening positron annihilation spectroscopy, the *S*-parameter is an empirical line-shape parameter defined as the fraction of annihilation events in the central part of the 511 keV peak, which is dominated by annihilations with low-momentum electrons. Although S is not a fundamental material constant, it provides a sensitive metric of changes in the electron momentum distribution sampled by the positron. Increases in S are typically linked to enhanced positron trapping at open-volume defects, which reduces the relative contribution from high-momentum core electrons.[51] Thus, in PAS measurements, a higher *S*-parameter generally indicates a higher concentration or larger size of vacancy-type defects in terms of positron trapping sites.[36] The characteristic depth dependence of the *S*-parameter also enables identification of spatial inhomogeneities in defect distribution, which is particularly useful in layered structures like epitaxial thin films.

In the as-grown samples shown in Fig. 3, the undoped $Mg_2Sn$ film exhibits a pronounced S peak of $0.62 \pm 0.01$ at $\approx$ 50 nm, indicative of a high density of Mg-vacancy clusters in the mid-film region, consistent with previous observations.[12,52] This depth-localized maximum suggests that vacancy formation is not uniform throughout the film thickness, likely reflecting kinetic factors during epitaxial growth. Such depth inhomogeneity can arise because defect formation conditions evolve during film growth and can differ between the near-surface region, the film interior, and the film-substrate interface. With increasing Li doping, the peak *S*-value decreases monotonically: $0.57 \pm 0.01$ for $x = 0.05$ Li content and $0.54 \pm 0.01$ for $x = 0.10$ Li content. This behavior suggests that Li incorporation during growth suppresses the formation of Mg-vacancy-type defects in the region where the undoped film shows the maximum. Although the microscopic mechanism cannot be determined from the *S*-parameter profiles alone, the reduced peak S indicates a weaker vacancy-type defect signal under Li-doped growth conditions.

The monotonic reduction in S with increasing Li is consistent with a Li-driven change in how non-stoichiometry and charge compensation are accommodated. XRD shows that increasing Li promotes β-Sn, indicating that a larger fraction of Sn is accommodated by segregation into a secondary phase rather than being retained within the $Mg_2Sn$ matrix. This can reduce the degree of matrix off-stoichiometry that would otherwise be accommodated by vacancy-type defects, which is consistent with a reduced vacancy-type PAS signature. In addition, Kamila *et al.*[46] describe compensating Li-related defects in $Mg_2Sn$, with Li on Mg sites acting as an acceptor and Li

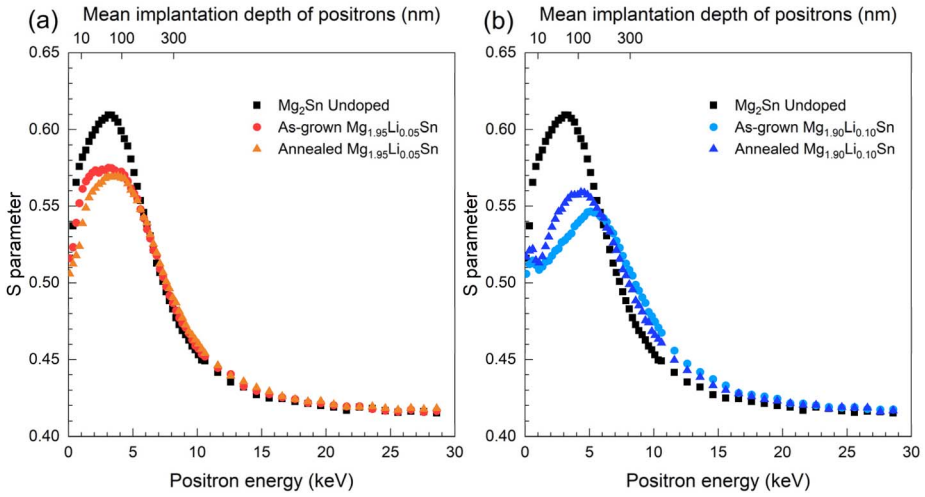


Fig. 3 Depth-resolved *S*-parameter profiles from positron-annihilation spectroscopy for $Mg_{2-x}Li_xSn$ films with (a) $x = 0.05$ and (b) $x = 0.10$, in as-grown and annealed states.

interstitials acting as a donor, and they show that compensation becomes more important at higher Li concentration and limits dopant efficiency. Because PAS reports on open volume and positron trapping efficiency, a shift toward compensated Li-related defects and Li-associated complexes can suppress the vacancy-type S signature even when the overall defect chemistry evolves.

Upon annealing, the evolution of the *S*-parameter varies depending on the Li content. In the $x = 0.05$ Li film in Fig. 3a, the *S*-parameter is slightly reduced, with the peak value dropping to $0.56 \pm 0.01$, accompanied by a 5–7% decline near the surface (<20 nm), while no significant change is observed near the interface region. These reductions reflect the effective migration and annihilation of vacancy-type defects, likely facilitated by thermally activated diffusion to sinks such as grain boundaries, dislocation cores, or interfaces involving Sn-rich regions. Although Sn-related phases identified in XRD do not act as sources of vacancies, their gradual suppression after annealing suggests they may participate in defect relaxation processes. This result implies that the decrease in vacancy-type defects could be linked to the partial dissolution or redistribution of Sn-rich segregated regions, which in turn enhances the pathways for vacancy elimination. The observed defect suppression in the $x = 0.05$ $Mg_{2-x}Li_xSn$ film is driven by two synergistic effects: a moderate initial vacancy density that supports vacancy mobility, and an annealing temperature sufficient to promote vacancy diffusion without triggering clustering or structural degradation. The spatial uniformity of the *S*-parameter reduction also points to bulk-wide defect recovery, possibly assisted by strain relaxation and local recrystallization mechanisms coinciding with the diminishing Sn secondary phases.

In contrast, the $x = 0.10$ Li sample in Fig. 3b exhibits a reversal of this trend. After annealing, the peak *S*-parameter increases to $0.56 \pm 0.01$, centered around the same depth (~50 nm) as in the as-grown state. This suggests that new open-volume defects form or that pre-existing vacancies become stabilized in regions where vacancy annihilation would otherwise be expected. One plausible explanation is that excess Li at this concentration becomes supersaturated and promotes the nucleation of Li-rich or Li–Sn defect complexes under thermal activation. These clusters could locally distort the lattice and act as positron traps, inhibiting the annihilation of native vacancies or introducing additional open-volume sites.

The depth sensitivity of PAS allows us to spatially resolve where such changes occur most significantly. Notably, both vacancy reduction in the $x = 0.05$ $Mg_{2-x}Li_xSn$ film and vacancy generation or stabilization in the $x = 0.10$ $Mg_{2-x}Li_xSn$ film are most prominent around 50 nm. This region may be particularly responsive to thermal treatment due to localized stress concentrations or defect diffusion gradients originating from the surface or the substrate interface.

### 3.3 Electrical transport from Hall measurements

Hall measurements shown in Fig. 4a and b reveal a clear evolution in carrier concentration and mobility as a function of Li content and thermal treatment. In the as-grown films, hole concentrations rise systematically with increasing Li, from ~$3.1 \times 10^{20}$ $cm^{-3}$ at $x = 0.05$ to ~$7.1 \times 10^{20}$ $cm^{-3}$ at $x = 0.10$. This trend confirms that Li atoms act as effective acceptors, primarily substituting on Mg sites ($Li_{Mg}$), while also reflecting the contribution of native Mg vacancies formed during the MBE growth. These defects, acting as shallow acceptors, could collectively result in elevated hole densities.

After annealing, all films exhibit a reduction in carrier concentration. For films with lower Li content ($x = 0.05$), this reduction is moderate and correlates well with the PAS-observed suppression of vacancy-type defects. However, in higher Li content films ($x = 0.10$), the drop in carrier concentration is considerably more pronounced, suggesting that additional mechanisms are at play. These may include the deactivation of Li-related shallow defects or the restructuring of complex defect environments involving Sn-rich phases. Mg vacancies, which are prominent in the as-grown films, are partially annihilated, contributing to the reduced acceptor density. In high Li content

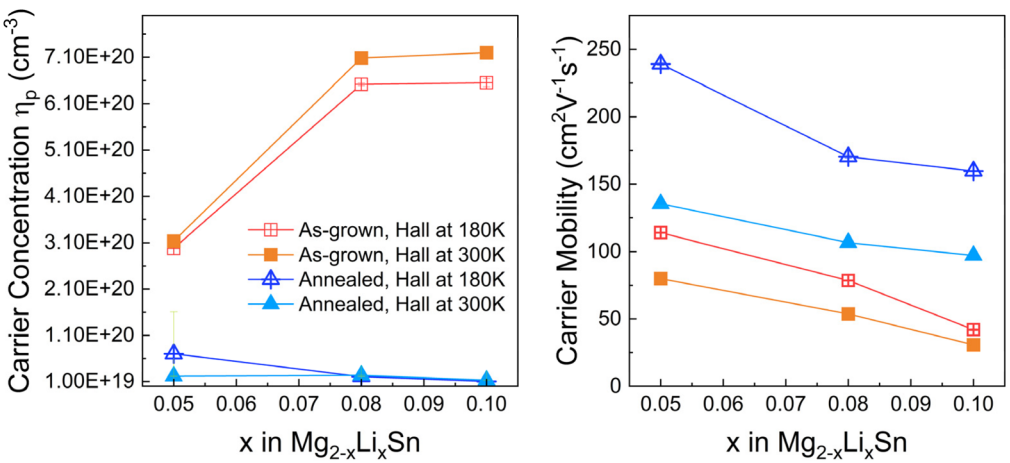


Fig. 4 Carrier concentration and mobility of $Mg_{2-x}Li_xSn$ films measured by Hall effect at 180 K and 300 K, shown for as-grown and annealed samples.

 

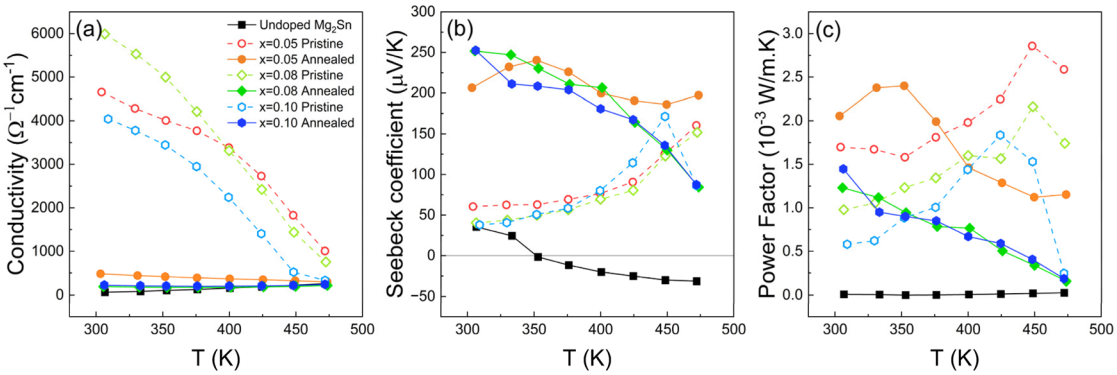


Fig. 5 Temperature dependence of (a) electrical conductivity, (b) Seebeck coefficient, and (c) power factor of $Mg_{2-x}Li_xSn$ films.

samples, the additional decrease in carrier concentration likely stems from the transformation of Li-related complexes, such as Li–Sn or Li-vacancy pairs into electrically inactive configurations. This interpretation is supported by PAS data showing the reappearance or stabilization of open-volume complexes in the $x = 0.10$ film after annealing, alongside the persistent Sn-rich phases identified by XRD.

Carrier mobility in Fig. 4b improves significantly across all doping levels following annealing. For $x = 0.05$, mobility increases from ~80 to ~135 $cm^2 \cdot V^{-1} \cdot s^{-1}$ at room temperature, while for $x = 0.10$, it rises from ~25 to ~100 $cm^2 \cdot V^{-1} \cdot s^{-1}$. These increases reflect a substantial reduction in ionized impurity and defect scattering. The strongest improvements are observed at moderate Li levels, where PAS indicates effective vacancy suppression and XRD shows minimal residual Sn phases. In contrast, at higher Li content, although mobility still increases, the gain is limited by the persistence of Sn-rich precipitates and complex defect structures, which likely act as residual scattering centers.

### 3.4 Thermoelectric properties

Temperature-dependent electrical conductivity measurements (Fig. 5a) reveal a distinct difference between as-grown and annealed Li-doped $Mg_2Sn$ films. In as-grown samples, conductivity is exceptionally high across all Li levels, with $x = 0.08$ reaching over 6000 $\Omega^{-1}$ $cm^{-1}$ at 300 K. However, this high conductivity gradually declines with temperature, exhibiting a weak metallic-like trend that becomes more pronounced with increasing Li content. This anomalous behavior arises from the combination of elevated carrier concentration and residual defect scattering, including Sn-rich inclusions that persist in the lattice. Following annealing, conductivity drops significantly across all compositions but exhibits a more thermally stable profile. The annealed films show conductivity values that remain within a moderate range over temperature, with $x = 0.05$ retaining the highest conductivity among the compositions. Minor variations in slope suggest overall improved thermal stability of electrical transport compared to the as-grown state. The suppressed conductivity post-annealing reflects the intentional reduction of carrier concentration as confirmed by Hall measurements, and the concurrent increase in mobility due to defect annihilation. This shift from degenerate-like to intrinsic transport indicates that annealing mitigates the dominant ionized impurity scattering in as-grown films, leading to more thermally stable electrical behavior.

The Seebeck coefficient in Fig. 5b shows a dramatic transformation upon annealing. As-grown films display relatively low $S$ values near room temperature, ranging from ~40 to 70 μV $K^{-1}$, and increase gradually with temperature. After annealing, $S$ increases sharply across the entire temperature range, reaching up to ~250 μV $K^{-1}$ for $x = 0.05$ and remaining above 150 μV $K^{-1}$ for higher Li levels, with a flatter and more consistent temperature dependence. This enhancement primarily reflects the annealing-induced reduction in hole concentration as confirmed by Hall measurements, which shifts the Fermi level away from the band edge and increases the thermopower. The concurrent mobility increase indicates reduced charged-defect disorder and suppression of ionized-impurity disorder, which improves the stability and reproducibility of the transport response. The higher Seebeck values, combined with more stable electrical conductivity, result in a substantial increase in power factors (Fig. 5c). The annealed $x = 0.05$ film achieves an exceptional peak power factor of ~$2.4 \times 10^{-3}$ $W \cdot m^{-1} \cdot K^{-2}$ at the relatively low temperature of ~350 K, significantly exceeding the previous benchmark of $1.48 \times 10^{-3}$ $W \cdot m^{-1} \cdot K^{-2}$ for Ga-doped $Mg_2Sn$ epitaxial films.[22] This result highlights the efficiency of Li doping and defect engineering by thermal treatment in producing high-performance p-type $Mg_2Sn$ without relying on rare or heavy dopants.

To verify whether the annealing-induced changes in transport behavior also improve reproducibility over repeated measurements, cyclic heating–cooling tests were performed on the $x = 0.05$ composition (SI Fig. S4). In the as-grown film, the Seebeck coefficient shifted between cycles, indicating changes in carrier concentration or scattering during initial heating. After annealing, both conductivity and Seebeck traces overlapped between cycles within experimental error, confirming that the post-growth treatment removes metastable defect states responsible for the observed cycle-to-cycle variation. Similar heating–cooling measurement protocols have also been employed in our previous studies on undoped, Ge-doped, and Ga-doped $Mg_2Sn$ films, as well as for the undoped $Mg_2Sn$ film

measured here.[21,22] In those cases, the Seebeck coefficient and electrical conductivity before and after temperature cycling showed only small, largely reversible changes, indicating that the pronounced irreversible changes discussed in this work are specific to Li-doped $Mg_2Sn$ and reflect the modification of Li-related defect states.

### 3.5 Thermal Conductivity and *zT* estimation

Thermal conductivity extracted from TDTR shown in Fig. 6 shows that in the unannealed state the Li-doped films exhibit relatively low $\kappa$. In the analysis, the $Mg_{2-x}Li_xSn$ layer was treated as a single $Mg_2Sn$-based film, and the fitted thermal diffusivity and effusivity were converted to $\kappa$ using bulk $Mg_2Sn$ density and heat capacity. The Sn-rich precipitate regions observed near the surface in Fig. 2 were therefore incorporated into this effective homogeneous layer rather than modeled as a separate phase. The suppressed $\kappa$ is attributed to strong phonon scattering by disordered vacancy-type defects, Sn-rich inclusions, and grain boundary disorder introduced during epitaxial growth, as supported by PAS and XRD. These structural inhomogeneities efficiently disrupt phonon transport but are simultaneously associated with unstable electronic transport.

On the other hand, annealing consistently increases $\kappa$ at all Li levels. $\theta$–$2\theta$ scans revealed a uniform rightward shift of the $Mg_2Sn(111)$ peak, indicating reduced lattice spacing. This contraction reflects more complete substitutional Li incorporation on Mg sites and the removal or reorganization of lattice-expanding defects and Sn-rich precipitates. The resulting structural changes have two dominant effects. First, secondary phases that act as strong scattering centers are partially dissolved or coarsened into fewer, larger inclusions, lowering the density of high-angle grain and phase boundaries encountered by heat-carrying phonons. Second, a more uniform Li distribution suppresses local compositional fluctuations and associated strain fields, promoting a more coherent bonding network. This enhanced bonding environment is expected to strengthen interatomic interactions, leading to higher acoustic phonon velocities and longer mean free paths, thereby improving lattice thermal conductivity.[53,54] Interestingly, in the $x = 0.10$ Li-doped film, PAS measurements show an increase in the *S*-parameter after annealing, suggesting a higher concentration or stabilization of open-volume defects. However, this does not result in lower thermal conductivity. While PAS is highly sensitive to open-volume defects, it does not distinguish isolated vacancies from larger, less-disruptive defect clusters. Hence, the observed increase in the *S*-parameter may stem from the formation of Li-rich defect complexes or residual Sn-rich clusters that trap positrons efficiently but are spatially localized and insufficiently coupled to phonon transport to significantly impact thermal conductivity.

In prior studies of compounds along the pseudo-binary $GeTe–Sb_2Te_3$ line, it was shown that disordered vacancies serve as potent phonon scatterers, drastically suppressing thermal conductivity.[55] Upon annealing, these vacancies undergo partial ordering, reducing their scattering strength and enabling more extended phonon transport. This leads to a transition from glass-like to more "crystal-like" thermal conductivity, where phonon behavior increasingly resembles that of a structurally coherent crystal despite the persistence of some defects. A similar mechanism may also be likely active in our Li-doped $Mg_2Sn$ films. The reorganization of point defects during annealing reduces phonon scattering from short-range disorder and promotes more coherent heat transport. Even if defect complexes remain, their impact becomes less pronounced in the more ordered lattice.

Despite the rise in $\kappa$ after annealing, the Li-doped $Mg_2Sn$ films maintain lower thermal conductivity than previously reported Ga-doped $Mg_2Sn$ and $Mg_2Sn(Ge)$ epitaxial thin films grown under similar conditions.[12,22,52] This indicates that lithium is more effective in maintaining phonon-disruptive disorder, even after thermal processing. The combination of structural recovery and retained phonon scattering supports the use of Li as an effective defect-engineering element in thin-film thermoelectric systems.

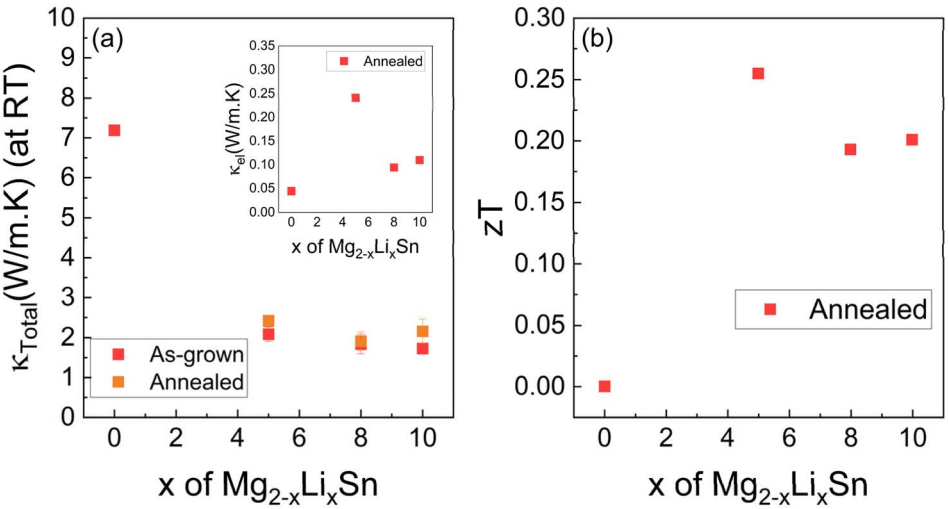


Fig. 6 (a) Total thermal conductivity and (b) estimated *zT* values for annealed $Mg_{2-x}Li_xSn$ films.

 

The $zT$ values are presented in Fig. 6b $zT$ was estimated only for the annealed films because the as-grown films do not provide measurement stable $S$ and $\sigma$, and therefore $zT$cannot be treated as a reliable material metric prior to annealing. In this estimation we combine the in-plane Seebeck coefficient and electrical conductivity with the cross-plane thermal conductivity obtained from TDTR under the assumption that $Mg_2Sn$-based films are isotropic in $\kappa$. This assumption is consistent with the cubic antifluorite structure of $Mg_2Sn$, which is generally regarded as isotropic in its thermal and electronic transport properties, so the reported $zT$ values should be viewed as effective values based on the measured cross-plane $\kappa$. The highest room-temperature $zT$ of ~0.25 is achieved for the $x$ = 0.05 Li film, surpassing the 0.08 reported for $Mg_2Sn_{0.97}Ga_{0.03}$ thin films,[22] and the ~0.06–0.14 range for bulk Na–, Li–, and Ag–doped $Mg_2Sn$.[56] Although lower than the 0.34–0.38 reported at 700 K for high-quality single crystals, which represents the highest reported value for p-type $Mg_2Sn$,[18,57,58] our value is notable for the much lower measurement temperature and the thin-film geometry, while retaining defect-engineered phonon scattering after annealing.

### 3.6 π-Type device demonstration

The optimized annealed $Mg_{2-x}Li_xSn$ ($x$ = 0.05) film was implemented as the p-type leg in a microfabricated in-plane π-type thermoelectric device, paired with Bi n-type legs. The device comprised 36 p–n pairs patterned on a sapphire(0001) substrate, with contacts formed by Cr/Ni/Pt metallization and Bi deposited by electron-beam evaporation at room temperature. Li-doped $Mg_2Sn$ legs were patterned *via* $BCl_3$/Ar plasma reactive ion etching, replacing the argon-ion milling and RIE sequence used in earlier work, which improved etch selectivity and yielded smoother sidewalls.

As shown in Fig. 7a and b, the microdevice exhibited stable thermoelectric operation from $\Delta T$ = 0–120 K. In these measurements, the in-plane temperature difference $\Delta T$ was evaluated using a differential thermocouple attached to the sapphire substrate near the hot and cold ends of the device, following the previous study.[44,45] Considering that the thin films have a very small heat capacity and are strongly thermally coupled to the substrate, their temperature is effectively governed by the substrate temperature; therefore, we use the substrate temperature difference as $\Delta T$ for the films. The output voltage–current lines and output power–current curves across the full $\Delta T$ range were linear and sharply peaked, respectively, indicating uniform current distribution and stable electrical interfaces. Fig. 8a shows the open-circuit voltage ($V_{OC}$) increasing linearly with $\Delta T$, reaching 0.76 V at $\Delta T$ = 120 K, without signs of contact degradation or thermal-mechanical failure. The corresponding maximum output power ($P_{max}$) in Fig. 8b exhibits a quadratic dependence on $\Delta T$, attaining 0.74 μW at $\Delta T$ = 120 K. Even at small $\Delta T$, the device produces measurable output: $V_{OC}$ = 0.0292 V and $P_{max}$ = 1.29 nW at $\Delta T$ = 5 K, confirming measurable conversion even at very small temperature differences. The short-circuit currents were 0.16 μA and 3.84 μA at $\Delta T$ = 5 and 120 K, respectively.

The maximum output power density ($P_{max\_density}$) in Fig. 8c increases sharply with $\Delta T$, reaching 12.1 mW cm$^{-2}$ at $\Delta T$ = 120 K. To enable a direct comparison with reported $\mu$-TEG performance metrics, we evaluate the $\Delta T^2$-normalized maximum output power density following the thin-film device analysis of Ohkubo *et al.*[45] The maximum normalized output power density ($P_{max\_density\_norm}$), shown in Fig. 8d, was calculated as $P_{max\_density\_norm} = P'_{max\_density} f/\Delta T^2$ where $P_{max\_density} = P_{max}/A_{legs}$ is referenced to the total cross-sectional area of the thermoelectric legs (sum of the p- and n-type leg cross-sections, $A_{legs}$) and $f$ is the filling factor, defined as $f = A_{legs}/A_{dev}$, the ratio of the total cross-sectional area of the thermoelectric legs to the total device area that converts the $P_{max\_density}$ to a device-footprint-referenced power density.[59] For the present device, $f$ = 0.94. The maximum normalized output power density remains nearly constant at ~0.80–0.82 μW cm$^{-2}$ K$^{-2}$ across the full temperature range, indicating that conversion efficiency is stable and not degraded by thermal or electrical contact resistance at high $\Delta T$.

While both $V_{OC}$ and $P_{max}$ are lower than in $Mg_2Sn$(Ge)-based devices fabricated in the same configuration,[44,45] this behavior may be mainly attributed to increased interface resistance. Thermally, contact resistance reduces the effective temperature drop across the legs and lowers the measured $V_{OC}$. Electrically,

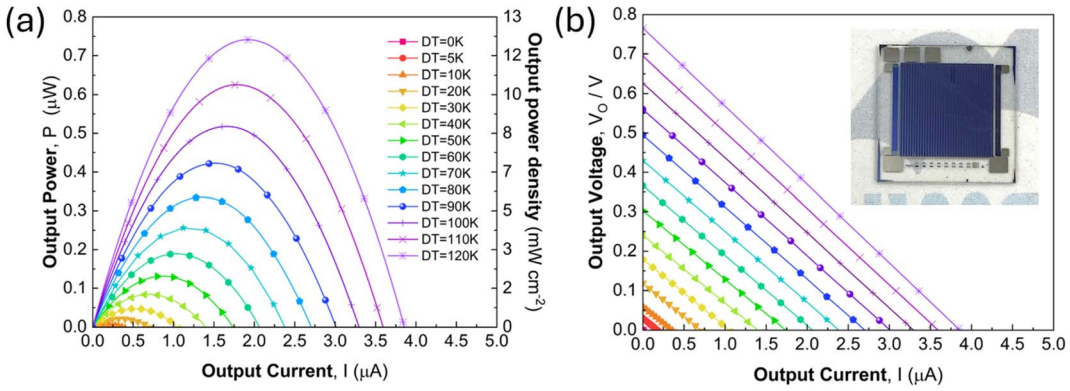


Fig. 7 (a) Output voltage and (b) power characteristics of a 36-p-*n*-pair π-type microdevice using $Mg_{1.95}Li_{0.05}Sn$ as p-type legs and Bi as n-type legs on sapphire(0001), measured in vacuum under various $\Delta T$.

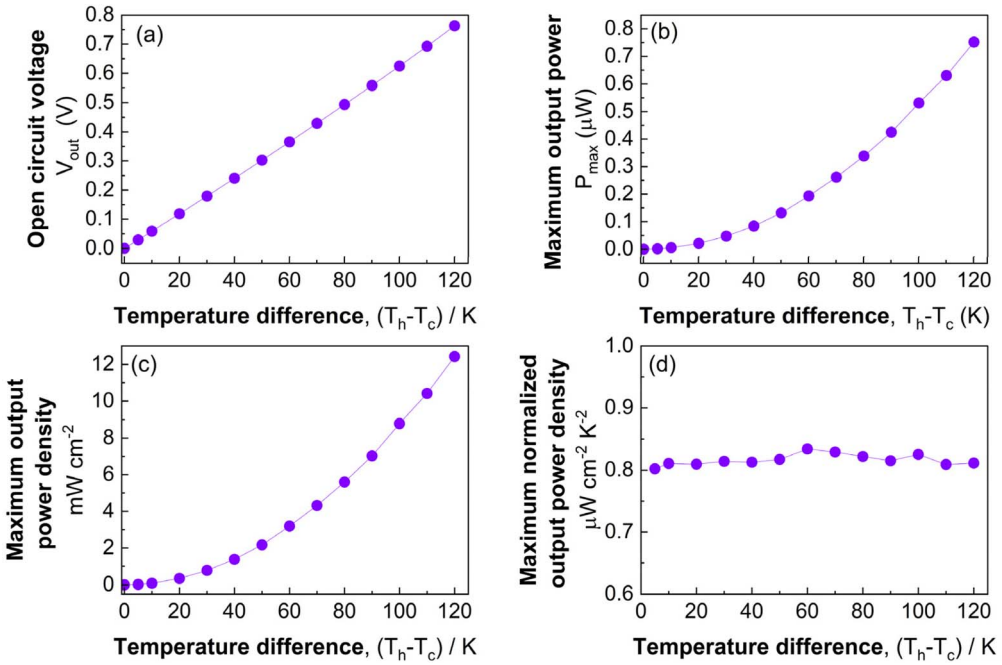


Fig. 8 (a) Open circuit voltage, (b) maximum output power, (c) maximum output power density, and (d) maximum normalized output power density plotted as functions of temperature difference for the $Mg_{1.95}Li_{0.05}Sn$/Bi π-type microdevice.

contact and junction resistances add series resistance under load and cap $P_{max}$ even when the power factor improves. To quantify this effect, the internal resistance $R_{int}$of the microdevice was measured is summarized in Fig. 9, showing an increase from ~160 × $10^3$ Ω near $\Delta T \approx 0$ K to ~200 × $10^3$ Ω at $\Delta T \approx 120$ K. Because the maximum power output scales as $P_{max} = V_{OC}^2/(4R_{int})$, the comparatively low normalized maximum output power density is therefore closely linked to the large internal resistance, rather than being limited solely by the intrinsic thin-film thermoelectric properties. Although the absolute power output is small for directly powering most IoT nodes, the device operates stably from $\Delta T = 5$ K to 120 K. A clear route to higher output is to minimize interface resistance through optimized contact metals, barrier layers, and junction geometry, together with scaling leg count and area or pairing with an n-type leg of larger $|S|$.[60]

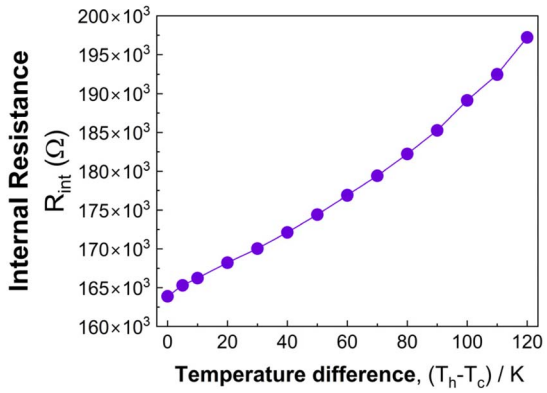


Fig. 9 Internal resistance of the TE microdevice as a function of temperature difference measured directly on the full device using the same two-terminal configuration as the output measurements.

## 4 Conclusions

We fabricated $Mg_{2-x}Li_xSn$ ($0 \le x \le 0.10$) epitaxial thin films and systematically investigated the effects of Li doping and post-growth annealing on their structure, defect landscape, and thermoelectric properties. Li incorporation suppressed Mg vacancies most effectively at $x = 0.05$, while higher doping induced surface-segregated Sn-rich precipitates that were only partially reabsorbed after annealing at 473 K. PAS confirmed vacancy passivation in the $x = 0.05$ film after annealing, correlating with a substantial mobility increase and the highest Seebeck coefficient (~250 μV $K^{-1}$) and power factor (~2.4 mW $m^{-1}$ $K^{-2}$ at 350 K) among all compositions. Thermal conductivity rose moderately after annealing due to improved lattice order, yet remained lower than in Ge- or Ga-doped analogues, enabling the highest $zT$ for the $x = 0.05$ Li film. A 36 p–n pair π-type microdevice based on this composition exhibited stable operation up to $\Delta T = 120$ K, validating its device-level reliability. These results establish Li-doped $Mg_2Sn$, optimized by moderate-temperature annealing, as a promising lead-free p-type material for micro-scale thermoelectric generators in IoT and on-chip cooling applications.

## Author contributions

Kenneth Magallon Senados: conceptualization, methodology, investigation, formal analysis, writing – original draft. Takashi Aizawa: conceptualization, methodology, resources,

 

investigation, formal analysis, writing – review & editing. Isao Ohkubo: conceptualization, methodology, resources, investigation, formal analysis, writing – review & editing. Masayuki Murata: methodology, resources, investigation, writing – review & editing. Takahiro Baba: methodology, investigation, formal analysis. Akihiko Ohi: methodology, resources, investigation. Akira Uedono: methodology, resources, investigation. Takeaki Sakurai: investigation, writing – review & editing, supervision. Takao Mori: conceptualization, funding acquisition, project administration, resources, writing – review & editing, supervision.

## Conflicts of interest

There are no conflicts to declare.

## Data availability

The authors declare that the data supporting the findings of this study are available within the paper and its supplementary information (SI). Supplementary information: additional experimental details and supporting characterization and transport data. See DOI: https://doi.org/10.1039/d5ta09301e.

## Acknowledgements

The work is supported by the JST Mirai Grant No. JPMJMI19A1. A part of this work was supported by "Advanced Research Infrastructure for Materials and Nanotechnology in Japan (ARIM)" of the Ministry of Education, Culture, Sports, Science and Technology (MEXT) Proposal Number JPMXP1224NM5157. We thank Noriyuki Okada for TEM specimen preparation and Makoto Oishi for TEM imaging. K.M.S. gratefully acknowledges financial support from the Japanese Government through the Monbukagakusho Scholarship.

## References

1 Q. Zhang, K. Deng, L. Wilkens, H. Reith and K. Nielsch, *Nat. Electron.*, 2022, **5**, 333–347.
2 S. Asadikouhanjani, A. Zolfagharian and M. Bodaghi, *Adv. Eng. Mater.*, 2024, **26**, 2301609.
3 Y. Li, G. Wang, M. Akbari-Saatlu, M. Procek and H. H. Radamson, *Front. Mater.*, 2021, **8**, 611078.
4 J. M. Sojo-Gordillo, D. Estrada-Wiese, A. Rodriguez-Iglesias, C. Duque-Sierra, M. Fernandez-Regulez, I. Martin-Fernandez, M. Salleras, L. Fonseca, A. Morata and A. Tarancón, *Adv. Funct. Mater.*, 2025, **35**, 2419639.
5 Z. Liu and T. Mori, System-Materials Nanoarchitectonics, in *NIMS Monographs*, ed. Y. Wakayama and K. Ariga, Springer, Tokyo, 2022, pp. 199–231.
6 I. Petsagkourakis, K. Tybrandt, X. Crispin, I. Ohkubo, N. Satoh and T. Mori, *Sci. Technol. Adv. Mater.*, 2018, **19**, 836–862.
7 Z. Hu, K. M. Senados, T. Sakurai, T. Aizawa and T. Mori, *Appl. Phys. Lett.*, 2025, **126**, 123102.
8 D. Enescu, in *Green Energy Advances*, IntechOpen, 2019.
9 M. A. Zoui, S. Bentouba, J. G. Stocholm and M. Bourouis, *Energies*, 2020, **13**, 3606.
10 *Thermoelectric Thin Films*, ed. P. Mele, D. Narducci, M. Ohta, K. Biswas, J. Morante, S. Saini and T. Endo, Springer International Publishing, Cham, 2019.
11 R. Venkatasubramanian, E. Siivola, T. Colpitts and B. O'Quinn, *Nature*, 2001, **413**, 597–602.
12 K. M. Senados, T. Aizawa, I. Ohkubo, T. Baba, A. Uedono, T. Sakurai and T. Mori, *J. Phys.: Energy*, 2025, **7**, 035001.
13 R. Santos, S. Aminorroaya Yamini and S. X. Dou, *J. Mater. Chem. A*, 2018, **6**, 3328–3341.
14 Q. Zhang, L. Cheng, W. Liu, Y. Zheng, X. Su, H. Chi, H. Liu, Y. Yan, X. Tang and C. Uher, *Phys. Chem. Chem. Phys.*, 2014, **16**, 23576–23583.
15 Y. Zhu, J. Li, B. Duan, Y. Li, P. Zhai and P. Li, *J. Mater. Sci.: Mater. Electron.*, 2017, **28**, 9535–9541.
16 W. Saito, K. Hayashi, Z. Huang, J. Dong, J.-F. Li and Y. Miyazaki, *ACS Appl. Mater. Interfaces*, 2020, **12**, 57888–57897.
17 K. Yin, X. Su, Y. Yan, Y. You, Q. Zhang, C. Uher, M. G. Kanatzidis and X. Tang, *Chem. Mater.*, 2016, **28**, 5538–5548.
18 H. Kamila, P. Sahu, A. Sankhla, M. Yasseri, H.-N. Pham, T. Dasgupta, E. Mueller and J. de Boor, *J. Mater. Chem. A*, 2019, **7**, 1045–1054.
19 Z. Huang, K. Hayashi, W. Saito, J. Pei, J.-F. Li and Y. Miyazaki, *J. Mater. Chem. A*, 2023, **11**, 2652–2660.
20 J. Tani, T. Shinagawa and M. Chigane, *J. Electron. Mater.*, 2019, **48**, 3330–3335.
21 M. S. L. Lima, T. Aizawa, I. Ohkubo, T. Sakurai and T. Mori, *Jpn. J. Appl. Phys.*, 2021, **60**, SBBF06.
22 M. S. L. Lima, T. Aizawa, I. Ohkubo, T. Baba, T. Sakurai and T. Mori, *Appl. Phys. Lett.*, 2021, **119**(254101).
23 I. Ohkubo, T. Aizawa, K. M. Senados, M. S. L. Lima, T. Sakurai and T. Mori, *Jpn. J. Appl. Phys.*, 2023, **62**, 108004.
24 K. Magallon Senados and R. Magdadaro Vequizo, *Mater. Today: Proc.*, 2018, **5**, 15174–15179.
25 G. Latronico, P. Mele, C. Sekine, P. S. Wei, S. Singh, T. Takeuchi, C. Bourgès, T. Baba, T. Mori, P. Manfrinetti and C. Artini, *Nanotechnology*, 2023, **34**, 115705.
26 M. V. Daniel, M. Friedemann, J. Franke and M. Albrecht, *Thin Solid Films*, 2015, **589**, 203–208.
27 K. Ide, K. Nomura, H. Hosono and T. Kamiya, *Phys. Status Solidi*, 2019, **216**, 1800372.
28 C. Jeengar, M. Tomar, K. Jindal, A. Sharma and P. K. Jha, *Mater. Sci. Semicond. Process.*, 2023, **153**, 107127.
29 O. Norimasa, T. Chiba, M. Hase, T. Komori and M. Takashiri, *J. Alloys Compd.*, 2022, **898**, 162889.
30 H. Huang, W. Luan and S. Tu, *Thin Solid Films*, 2009, **517**, 3731–3734.
31 N. Hatsuta, D. Takemori and M. Takashiri, *J. Alloys Compd.*, 2016, **685**, 147–152.
32 Z. He, Y.-X. Chen, Z. Zheng, F. Li, G. Liang, J. Luo and P. Fan, *Ceram. Int.*, 2020, **46**, 13365–13371.
33 H. Y. Xu, Y. N. Guo, Y. Wang, J. Zou, J. H. Kang, Q. Gao, H. H. Tan and C. Jagadish, *J. Appl. Phys.*, 2009, **106**, 083514.

34 W. Li, J. Shi, K. H. L. Zhang and J. L. MacManus-Driscoll, *Mater. Horiz.*, 2020, **7**, 2832–2859.
35 T. Aizawa, I. Ohkubo, M. S. L. Lima, T. Sakurai and T. Mori, *J. Vac. Sci. Technol., A*, 2019, **37**, 061513.
36 F. Tuomisto and I. Makkonen, *Rev. Mod. Phys.*, 2013, **85**, 1583–1631.
37 A. Uedono, S. Ishibashi, N. Oshima and R. Suzuki, *Jpn. J. Appl. Phys.*, 2013, **52**, 08JJ02.
38 A. Uedono, W. Ueno, T. Yamada, T. Hosoi, W. Egger, T. Koschine, C. Hugenschmidt, M. Dickmann and H. Watanabe, *J. Appl. Phys.*, 2020, **127**, 054503.
39 A. Uedono, S. Ishibashi, K. Tenjinbayashi, T. Tsutsui, K. Nakahara, D. Takamizu and S. F. Chichibu, *J. Appl. Phys.*, 2012, **111**, 014508.
40 T. Baba, T. Baba, K. Ishikawa and T. Mori, *J. Appl. Phys.*, 2021, **130**, 225107.
41 T. Baba, *Jpn. J. Appl. Phys.*, 2009, **48**, 05EB04.
42 T. Baba, T. Baba and T. Mori, *Int. J. Thermophys.*, 2024, **45**, 61.
43 B. C. Gerstein, P. L. Chung and G. C. Danielson, *J. Phys. Chem. Solids*, 1966, **27**, 1161–1165.
44 I. Ohkubo, M. Murata, M. S. L. Lima, T. Sakurai, Y. Sugai, A. Ohi, T. Aizawa and T. Mori, *Mater. Today Energy*, 2022, **28**, 101075.
45 I. Ohkubo, M. Murata, A. Ohi, M. S. L. Lima, T. Sakurai, T. Aizawa and T. Mori, *Appl. Phys. Lett.*, 2023, **122**, 243901.
46 H. Kamila, B. Ryu, S. Ayachi, A. Sankhla, E. Mueller and J. de Boor, *J. Phys.: Energy*, 2022, **4**, 035001.
47 *CRC Handbook of Chemistry and Physics*, ed. W. M. Haynes, CRC Press, Boca Raton, FL, 97th edn, 2016.
48 H. Y. Chen and N. Savvides, *J. Electron. Mater.*, 2010, **39**, 1792–1797.
49 D. Fang, X. Cheng, Y. Li and Z. Sun, *RSC Adv.*, 2016, **6**, 96327–96333.
50 D. Suthar, Himanshu, R. Sharma, G. Chasta, S. L. Patel, S. Chander and M. S. Dhaka, *Phys. E*, 2022, **138**, 115117.
51 I. Makkonen and F. Tuomisto, *J. Appl. Phys.*, 2024, **135**, 040901.
52 K. M. Senados, M. S. L. Lima, T. Aizawa, I. Ohkubo, T. Baba, A. Uedono, T. Sakurai and T. Mori, *Jpn. J. Appl. Phys.*, 2024, **63**, 02SP40.
53 S. Hasan, P. Adhikari, S. San and W.-Y. Ching, *Sci. Rep.*, 2023, **13**, 16218.
54 S. Nayeb Sadeghi, S. M. Vaez Allaei, M. Zebarjadi and K. Esfarjani, *J. Mater. Chem. C*, 2020, **8**, 15705–15716.
55 K. S. Siegert, F. R. L. Lange, E. R. Sittner, H. Volker, C. Schlockermann, T. Siegrist and M. Wuttig, *Rep. Prog. Phys.*, 2015, **78**, 013001.
56 J. Tani, T. Shinagawa and M. Chigane, *J. Electron. Mater.*, 2019, **48**, 3330–3335.
57 H. Y. Chen, N. Savvides, T. Dasgupta, C. Stiewe and E. Mueller, *Phys. Status Solidi*, 2010, **207**, 2523–2531.
58 Z. Huang, K. Hayashi, W. Saito, J. Pei, J.-F. Li and Y. Miyazaki, *J. Mater. Chem. A*, 2023, **11**, 2652–2660.
59 Q. Zhang, K. Deng, L. Wilkens, H. Reith and K. Nielsch, *Nat. Electron.*, 2022, **5**, 333–347.
60 R. Chetty, J. Babu and T. Mori, *Joule*, 2024, **8**, 556–562.